



ELSEVIER

Available online at www.sciencedirect.com
jmr&t
 Journal of Materials Research and Technology
journal homepage: www.elsevier.com/locate/jmrt

Original Article

Fe₃O₄/Co₃O₄–TiO₂ S-scheme photocatalyst for degradation of organic pollutants and H₂ production under natural sunlight



M.M. Abutalib ^a, Haifa Mohammed Alghamdi ^a, A. Rajeh ^b, Omer Nur ^c,
 A.M. Hezma ^d, Mohammed A. Manna ^{e,*}

^a University of Jeddah, College of Science, Department of Physics, Jeddah, Saudi Arabia

^b Physics Department, Faculty of Science, Amran University, Yemen

^c Department of Science and Technology, Campus Norrkoping, Linkoping University, SE-601 74, Norrköping, Sweden

^d Spectroscopy Department, Physics Research Institute, National Research Center, Giza, Egypt

^e Chemistry Department, Faculty of Science, Amran University, Amran, Yemen

ARTICLE INFO

Article history:

Received 18 May 2022

Accepted 13 July 2022

Available online 31 July 2022

Keywords:

Fe₃O₄/Co₃O₄–TiO₂ nanoparticles

Multivalent states

Photocatalysis

S-Scheme mechanism

Tetracycline

Phenol

Hydrogen production

ABSTRACT

Sunlight responsible mono- and co-doped TiO₂ nanoparticles (Coⁿ⁺ and Feⁿ⁺) were prepared via sol–gel technique. The X-ray diffraction (XRD) results showed no phase change of TiO₂ was observed after the addition of Coⁿ⁺ and Feⁿ⁺ ions. Diffuse reflectance spectra (DRS) results showed a significant red-shift of the absorption edge after doping TiO₂ by Coⁿ and Feⁿ⁺ and the band gap energy reduced sharply from 3.10 to 1.72 eV. X-ray photoelectron spectroscopy (XPS) results emphasized the existence of multivalent states of Co²⁺, Co³⁺, Fe²⁺ and Fe³⁺. The results of ultraviolet photoelectron spectroscopy (UPS), work function, electron spin resonance (ESR) illustrated the Fe₃O₄/Co₃O₄–TiO₂ formed of ternary heterojunctions. The photocatalytic performance of the prepared photocatalysts was determined for photodegradation of tetracycline (TC) and phenol (P) and production of hydrogen. The results illustrated the existence of multivalent states of Fe and Co ions (Co²⁺, Co³⁺, Fe²⁺ and Fe³⁺) together improved the solar light absorption, inhibited the recombination of photo-generated charges and consequently enhanced the photocatalytic efficiency of TiO₂ compared with mono-doped TiO₂ (Co₃O₄/TiO₂ and Fe₃O₄/TiO₂). The sample with 5%Fe₃O₄/Co₃O₄–TiO₂ showed the highest photoactivity. The mineralization (TOC), photodegradation mechanism and reusability of prepared photocatalysts were also studied. The Fe₃O₄/Co₃O₄–TiO₂ nanoparticles showed high photoactivity and stability and can be adopted as a promising materials for different environmental and H₂ production applications.

© 2022 The Author(s). Published by Elsevier B.V. This is an open access article under the CC BY-NC-ND license (<http://creativecommons.org/licenses/by-nc-nd/4.0/>).

* Corresponding author.

E-mail address: mnnaam@yahoo.com (M.A. Manna).

<https://doi.org/10.1016/j.jmrt.2022.07.078>

2238-7854/© 2022 The Author(s). Published by Elsevier B.V. This is an open access article under the CC BY-NC-ND license (<http://creativecommons.org/licenses/by-nc-nd/4.0/>).

1. Introduction

In recent years, global energy demand increased rapidly due to the rapid growing of population and industrialization and led to appearing of different environmental problems [1–6]. Several efforts have been exerted to find a sustainable and efficient clean energy source as alternative source of fossil fuels and also ecofriendly [1,7,8]. Solar energy is clean and sustainable energy and could availing for production of hydrogen from water splitting as clean energy and also environmentally friendly and for waste water treatment of different environment pollutants [5,7,9,10]. Semiconductors nanocrystals have been applied as a promising approach for production of hydrogen and for solving and controlling on the environmental pollution [11,12]. Different efforts have been exerted to improving the photocatalytic properties of photocatalysts under solar light energy [13–15]. TiO_2 is one of the most important photocatalysts which attracted enormous attention for the environmental cleanup, solar energy conversion, hydrogen production and gas sensors due to its unique properties as high photochemical stability, special optoelectronic properties, nontoxicity, low-cost and high photocatalytic activity [16–18]. However; the major drawback of utilizing TiO_2 as photocatalyst under solar light illumination is its large bandgap (3.2 eV for anatase, 3.0 eV for rutile) where only about 4%–5% of the solar energy consists of UV light as well as the fast recombination of photo-generated $e^- - h^+$ pairs which largely hindered its practical application [16,19–21]. Different strategies have been developed to overcome on these drawbacks by modification the electronic structure of TiO_2 to absorb the visible light and be able to utilize a higher portion of the solar spectrum, including decoration, doping and coupling with other metals, non-metals ions and metal oxides [22,23]. However, the doping of 3 d-transition metals into TiO_2 can lead to heterojunctions with narrow the band gap of TiO_2 due to creation of new states which effectively improves the absorption in the visible light leading high catalytic efficiency in the visible light [24].

Different mechanisms have been proposed to describe the pathway charge carriers through photocatalysts heterojunctions, type II, Schottky junctions, and Z-scheme heterostructures [25–27]. However, different limitations and disadvantages conclusions resulted during application of these mechanisms to describe the charge transfer through the heterojunctions [26,28]. Therefore, S-scheme heterojunctions mechanism has been proposed as a suitable solution for these limitations and disadvantages explanations that induced by the previous photoactive mechanisms. In this mechanism, the heterojunction composed of two or more semiconductors, coupled with each other i.e., composed of a reduction photocatalyst (RP) and an oxidation photocatalyst (OP) [27,29]. However, the powerful photogenerated electrons and holes are remain in the CB of RP and VB of OP, respectively, while the useless photogenerated electrons and holes are recombined, leading a strong redox potential [30]. The pollutants that resulted from the industrial processes such as antibiotics, dyes, pigments, inksetc. led to appearing of different environmental problems which caused different

problems to microorganisms, aquatic environments, and human beings [31–36]. The photodegradation of organic pollutants is one of the most popular and important methods due to its advantage as effectiveness method, low cost and simplicity of operation [37–39].

In this work we prepared new ternary heterojunction $\text{Fe}_3\text{O}_4/\text{Co}_3\text{O}_4-\text{TiO}_2$ with S-scheme mechanism able to absorbed the solar energy as available and sustainable natural energy source in treatment of waste water for removal the organic pollutants and generation of H_2 as clean energy, eco-friendly and alternative energy source. Also, study the effect of electronic states of dopants and dopants content on the structural, morphological and optical properties of TiO_2 and reflection of these changes on the photocatalytic activity of TiO_2 . The photocatalytic performance of the prepared samples was investigated for degradation of TC and Pl and for H_2 production.

2. Experimental

2.1. Samples preparation

TiO_2 , $\text{Co}_3\text{O}_4-\text{TiO}_2$, $\text{Fe}_3\text{O}_4/\text{TiO}_2$ and $\text{Fe}_3\text{O}_4/\text{Co}_3\text{O}_4-\text{TiO}_2$ nanoparticles were prepared by simplest sol–gel technique. Typically [40]: 2.0 gm of CTAB was dissolved in 30 ml of ethanol and then 12 ml of titanium (IV) isopropoxide was added with constant stirring for 1 h. Next, 0.25 gm of $\text{Co}(\text{NO}_3)_3 \cdot 6\text{H}_2\text{O}$ and definite masses of $\text{Fe}(\text{NO}_3)_3 \cdot 9\text{H}_2\text{O}$ according to the required amount of iron dopant were dissolved in 20 ml of ethanol and then transferred to the above solution with continuous stirring for 2 h. Then, 10 ml of ammonia solution was added and stirred vigorously for 0.5 h. Afterward, the solution was left in the air overnight and the resulted gel was filtered, washed with deionized water and then dried at 80 °C for 8 h. Finally, the powder was calcined at 500 °C for 3 h. Similarly Co-doped TiO_2 was prepared without addition of $\text{Fe}(\text{NO}_3)_3 \cdot 9\text{H}_2\text{O}$ and TiO_2 without addition of $\text{Fe}(\text{NO}_3)_3 \cdot 9\text{H}_2\text{O}$ and $\text{Co}(\text{NO}_3)_3 \cdot 6\text{H}_2\text{O}$.

2.2. Characterization

The XRD patterns of the prepared photocatalysts were obtained on a PW Philips 1830. The Fourier transform infrared (FTIR) spectra were determined using a Shimadzu FTIR spectrometer. The morphology of the prepared photocatalysts was obtained using TEM using a JEOL-JEM-2100. Elemental composition study was achieved using energy dispersive X-ray (EDS) spectroscope equipped on SEM instrument. DRS analysis was recorded on a Shimadzu spectrophotometer (UV3600, Japan). XPS analysis was performed on a Microtech electron spectrometer. The photoluminescence (PL) spectra of were obtained using JASCO F.P.–750 Model, (Japan) spectrofluorometer.

2.3. Catalytic activity measurements

2.3.1. Photodegradation of pollutants

The photocatalytic activity of the prepared samples was investigated by degradation of TC and Pl under sunlight

illumination. The photoreactions were achieved in reactor surrounded with a cooling-water system. In this method, 0.05 g of photocatalyst powder was transfer into 50 ml of pollutant solution ($\text{Co} = 10 \text{ mg. L}^{-1}$). The photoreactions were achieved in sunny days from 11.5 a.m. to 2.5 p.m. In the beginning, the mixture was stirred in dark for 30 min and then transfer under the sunlight illumination with continuous and stable stirring. The degradation of pollutant was checked at regular intervals by taken 2 ml of the solution and then centrifuged to separate the photocatalyst powder and the remaining concentration of pollutant determined on a Shimadzu, MPC-2200 UV-vis spectrophotometer.

To investigate the active species that played the active role in the degradation of TC and Pl, different scavengers (1 mM) were added to the reaction mixture including Na_2EDTA , benzoquinone (BQ) and isopropanol (IPA) as scavengers of h^+ , $\cdot\text{O}_2^-$, and $\cdot\text{OH}$, respectively [41,42].

Also, the mineralization of the pollutants was investigated by total organic carbon (TOC) measurements using a Shimadzu-VCSN TOC analyzer. After the photodegradation, the %TOC of pollutant was estimated using the following equation:

$$\% \text{TOC} = \left(\frac{\text{TOC}_{\text{Initial}} - \text{TOC}_{\text{Final}}}{\text{TOC}_{\text{Initial}}} \right) \times 100 \quad (1)$$

2.3.2. Hydrogen production

The production of H₂ from water splitting was carried out under simulated sunlight using 150 W Xe lamp equipped with UV cutoff filter ($\lambda > 400 \text{ nm}$). Typically, 0.02 g of the photocatalyst powder was dispersed into 100 ml of 25 vol.% ethanol–water mixture in a Quartz reactor under magnetic stirring. Prior to start, gases in the reactor was removed by passing of N₂ gas through the reactor. The evolved H₂ gas was collected in gas bags, and were analyzed on GC-2014

(Shimadzu) equipped with a molecular sieve and Porapak Q column connected to TCD detector.

3. Results and discussion

3.1. XRD analysis

The XRD patterns spectra of TiO_2 , $\text{Co}_3\text{O}_4-\text{TiO}_2$, $\text{Fe}_3\text{O}_4/\text{TiO}_2$ and $\text{Fe}_3\text{O}_4/\text{Co}_3\text{O}_4-\text{TiO}_2$ nanoparticles are shown in Fig. 1. XRD pattern spectrum of TiO_2 shows diffraction peaks located at 25.28° , 38.75° , 48° , 55.7° , 62.04° , 68.96° , 70.4° and 75.2° indicating the presence of well crystalline of anatase structural phase (JCPDS# 21-1272) [43–45]. Also, a small peak observed at 27.5° attributes to the rutile phase. The diffraction peaks of $\text{Co}_3\text{O}_4-\text{TiO}_2$ and $\text{Fe}_3\text{O}_4/\text{Co}_3\text{O}_4-\text{TiO}_2$ nanoparticles (Fig. 1) showed the same characteristic peaks as TiO_2 and no phase change was observed after the addition process of cobalt and iron ions. This indicates that the addition of Co and Fe ions conserved the initial crystal structure of TiO_2 and enhanced the stability of the anatase phase through inhibition of anatase to rutile phase transformation [16,46]. Further, the intensity of diffraction peaks decreased gradually with increasing the Fe_3O_4 amount and no diffraction peaks attributed to Fe_3O_4 were observed with increasing the Fe_3O_4 content up to 5 wt.%, indicating the high dispersion and incorporation of Fe ions into the TiO_2 lattice [16,47]. However, new small peaks were detected in the sample with 10 wt.% Fe_3O_4 , indicating that some of the Fe ions precipitated out on the surface of TiO_2 [48]. The small peak that appeared at 35.8° indicates to the formation of Fe_3O_4 [49,50]. On the other hand, Fig. S1 (Supplementary information) displayed shift of anatase peaks (101) to higher angles after the addition of cobalt and iron ions into the TiO_2 . This observation can be ascribed to the

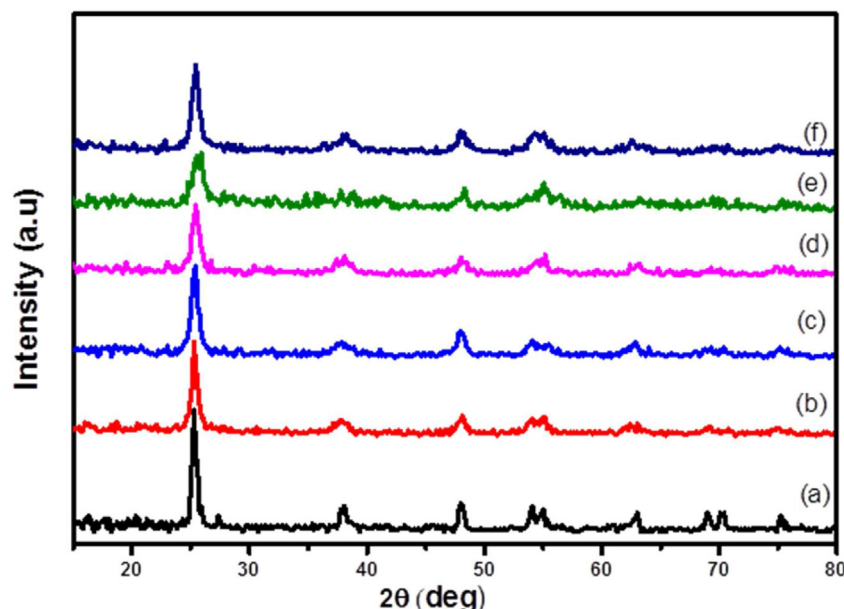


Fig. 1 – XRD patterns of (a) TiO_2 (b) $\text{Co}_3\text{O}_4/\text{TiO}_2$ (c) 2% $\text{Fe}_3\text{O}_4/\text{Co}_3\text{O}_4-\text{TiO}_2$ (d) 5% $\text{Fe}_3\text{O}_4/\text{Co}_3\text{O}_4-\text{TiO}_2$ (e) 10% $\text{Fe}_3\text{O}_4/\text{Co}_3\text{O}_4-\text{TiO}_2$ (f) 5% $\text{Fe}_3\text{O}_4/\text{TiO}_2$ nanoparticles.

shrinkage of unit cell of TiO_2 after the addition of Co and Fe ions which proves the replacement and substitution of some Ti ions by Co and Fe ions due to the similar radius of Co^{2+} (0.61 Å) and Fe^{3+} (0.64 Å) to that of Ti^{4+} (0.68 Å) which confirmed the incorporation of Co and Fe ions in the TiO_2 lattice [16,46,51,52].

The crystallites size of samples were calculated using Scherer's equation and the results were listed in Table 1. From Table 1, the crystallites size decreased gradually with increasing the Fe_3O_4 amount, indicating that the addition of Co and Fe ions reduced the grain growth of TiO_2 due to the suppressing impact of Co and Fe ions on the crystallite growth of TiO_2 causing reduction in the size of the crystals [46,47]. In comparison, the crystals size of 5% $\text{Fe}_3\text{O}_4/\text{TiO}_2$ was determined (Table 1) and the results showed that the crystals size of 5% $\text{Fe}_3\text{O}_4/\text{TiO}_2$ was larger than that of 5% $\text{Fe}_3\text{O}_4/\text{Co}_3\text{O}_4-\text{TiO}_2$ indicating the presence of Co and Fe ions together are more active in hindering the grain growth of TiO_2 compared with Fe ions alone.

3.2. TEM analysis

The morphologies of TiO_2 , $\text{Co}_3\text{O}_4-\text{TiO}_2$, $\text{Fe}_3\text{O}_4/\text{TiO}_2$ and $\text{Fe}_3\text{O}_4/\text{Co}_3\text{O}_4-\text{TiO}_2$ nanoparticles were studied as presented in Fig. 2. The images display that the samples have spherical shapes morphology and the average particles size varying in the range from 10 to 21 nm. Also, the images shows that the particles size decreased after the addition of Co and Fe ions and the sample with 5 wt.% of Fe_3O_4 amount showed the smallest particles size (Fig. 2(b) and (c)). In addition, the images illustrate that the aggregation ratio of the particles decreased after the addition of Co and Fe ions to the TiO_2 compared with TiO_2 . On the other hand, the particles size of 5% $\text{Fe}_3\text{O}_4/\text{TiO}_2$ nanoparticles (Fig. 2(d)) showed as spherical particles with size larger than that of 5% $\text{Fe}_3\text{O}_4/\text{Co}_3\text{O}_4-\text{TiO}_2$ nanoparticles. These observations are almost the same as that observed in the XRD results.

3.3. FTIR analysis

The FTIR spectra of pure and doped TiO_2 are shown in Fig. 3. In the spectra, broad peaks appeared at 3420, 1627 and 1382 cm^{-1} attributed to the stretching and bending vibrations of $-\text{OH}$ and adsorbed water on the samples surface [41,53,54]. The FTIR spectrum of pure TiO_2 (Fig. 3(a)) displayed broad absorption in the region of 400–900 cm^{-1} attributed to the stretching vibration of $\text{Ti}-\text{O}$ and $\text{Ti}-\text{O}-\text{Ti}$ bonds [23,42]. In

addition, the band at 1040 cm^{-1} attributes to the bridging stretching of $\text{Ti}-\text{O}-\text{Ti}$ bonds [23]. The FTIR spectrum of $\text{Co}_3\text{O}_4-\text{TiO}_2$ (Fig. 3(b)) showed two absorption bands located at 666 and 585 cm^{-1} attributed to the $\text{Co}^{2+}-\text{O}$ and $\text{Co}^{3+}-\text{O}$ vibrations which confirms the spinel structure of Co_3O_4 [55–57]. Further, Fig. 3(c)–(f) displayed that the addition of Fe_3O_4 led to appearance of bands at around 480, 430 and 541 cm^{-1} could be attribute to the vibrations of $\text{Fe}-\text{O}$ modes [58] while the band at 1060 cm^{-1} attributed to the $\text{Ti}-\text{O}-\text{Fe}$ [59]. Also, Fig. 3 showed that the intensity of these bands increased with increasing the Fe_3O_4 amount. It's reported that, the broad absorption band between 420 and 750 cm^{-1} indicates to the incorporation of dopants in the TiO_2 lattice and formation of Metal–O–Ti bonds [60]. Compared with undoped TiO_2 , Fig. 3 displayed small deviation in the bands positions under 1627 cm^{-1} after the addition of Co and Fe ions indicating the introducing of Co and Fe ions in the TiO_2 lattice and formation of $\text{Ti}-\text{O}-\text{Co}$ and $\text{Ti}-\text{O}-\text{Fe}$ network [53,60,61]. On the other hand, the intensity of the band at 666 cm^{-1} enhanced after the addition of Fe_3O_4 indicating the overlapping of this band with the absorption band that resulted from the $\text{Fe}-\text{O}$ band [48,62].

3.4. XPS analysis

Figure 4 displays the full range survey XPS spectra of 10% $\text{Fe}_3\text{O}_4/\text{Co}_3\text{O}_4-\text{TiO}_2$ nanoparticles are displayed in Fig. 4. The main peaks indicates to existence of Ti, Fe, Co, C and O elements detected at 458.37 (Ti2p), 712.21 (Fe2p), 783.04 (Co2p), 287.19 (C1s) and 530.2 eV (O1s) as shown in Fig. 4(a). From Fig. 4(b), the high-resolution scan of Ti2p region spectrum showed the presence of main doublet composed of two peaks at 458.13 eV and 464.2 eV assigned to Ti^{2+} and Ti^{3+} , respectively, which arise from spin-orbit splitting and existence of Ti^{4+} in the TiO_2 lattice [63,64]. Also, two peaks appeared at 457.68 eV and 463.38 eV assigned to Ti^{2+} and Ti^{3+} indicating the formation of Ti^{3+} [65]. Another peak appeared at 459.48 eV assigned to the formation of M–Ti–O (M = Fe or Co ions) which indicate to incorporation of Mn⁺ into the lattice of TiO_2 [22,66,67]. The high-resolution spectrum of Fe 2p (Fig. 4(c)) shows peaks appeared at 710.74 eV with its satellite at 717.66 eV and 713.5 eV with its satellite at 720.53 eV attributed to Fe^{2+} and Fe^{3+} , respectively [58,68]. Also, another peaks appeared at 724.07 and 726.85 eV (satellite), attributed to Fe^{2+} [69]. Another satellite peaks appeared at 730.25 and 733.95 eV attributed to valence interband transitions. These results indicate to the existence of Fe^{2+} and Fe^{3+} oxides [47]. The high-resolution spectrum of Co2p (Fig. 4(d)) displayed peaks appeared at binding energy around 780.53 and 792.43 eV with two satellite peaks at 786.12 and 801.22 eV, respectively, indicating the existence of Co^{3+} oxidation states while the peaks at 782.85 and 796.78 eV with two satellite peaks at 788.9 and 803.89 eV, respectively, verifying the existence of Co^{2+} oxidation states in the sample [70–72]. It was reported that the presence of Co^{3+} species in the sample generates more anionic defects, producing excess surface oxygen which in turn improves the photocatalytic activity [72]. On the other hand, Co^{2+} can incorporate in the TiO_2 lattice due to the ionic radius Co^{2+} is 0.65 Å which nearly has the same ionic radius as that of Ti^{4+} (0.68 Å) [73]. The O 1s

Table 1 – Textural properties and optical properties of the prepared photocatalysts.

Sample name	Crystallite size D (nm)	Band gap energy (eV)
TiO_2	18.5	3.10
2% $\text{Co}_3\text{O}_4-\text{TiO}_2$	16.7	2.53
2% $\text{Fe}_3\text{O}_4/\text{Co}_3\text{O}_4-\text{TiO}_2$	14.6	2.32
5% $\text{Fe}_3\text{O}_4/\text{Co}_3\text{O}_4-\text{TiO}_2$	13.4	1.85
10% $\text{Fe}_3\text{O}_4/\text{Co}_3\text{O}_4-\text{TiO}_2$	11.6	1.72
5% $\text{Fe}_3\text{O}_4/\text{TiO}_2$	15.2	2.10

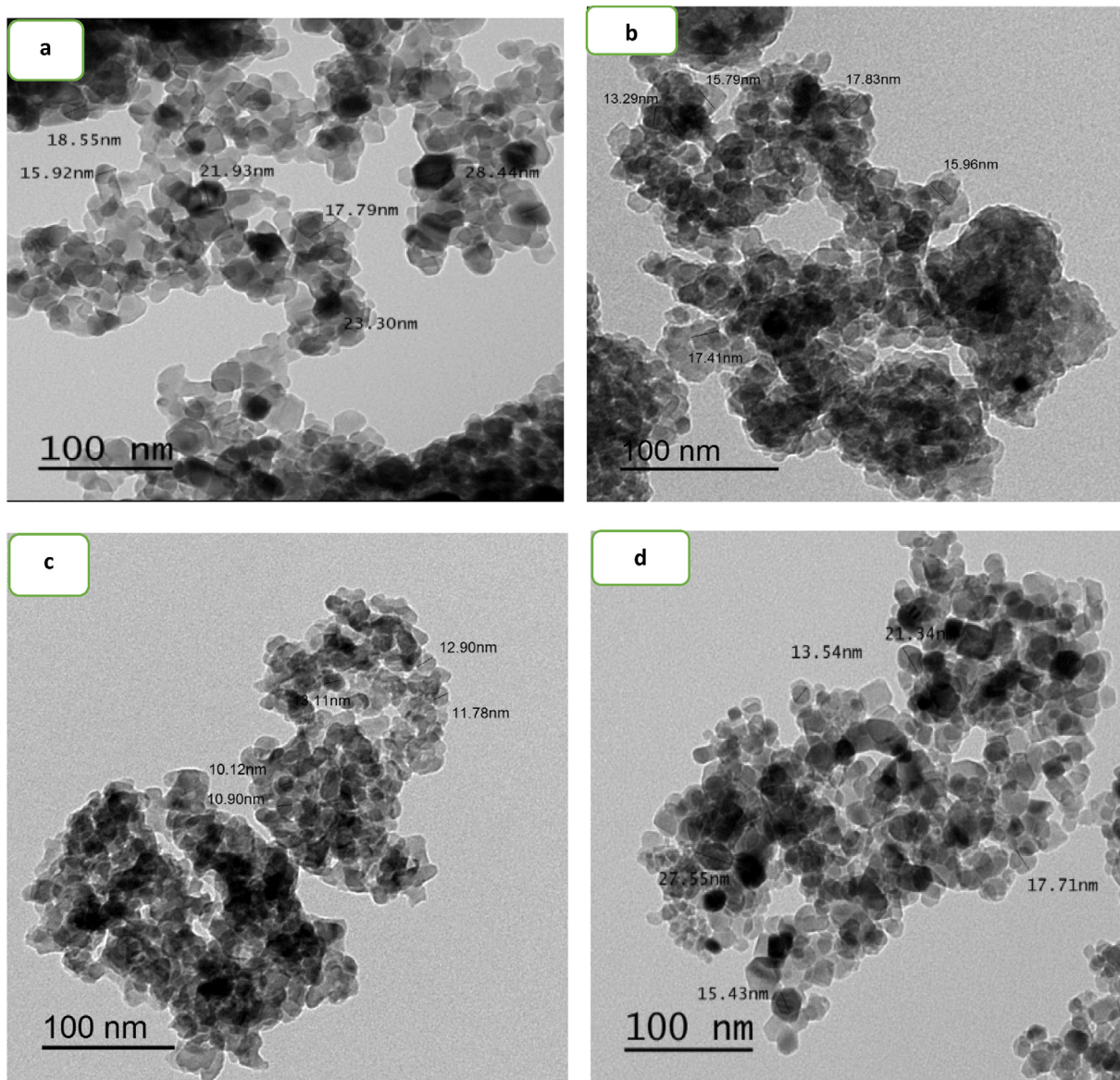


Fig. 2 – TEM images of (a) TiO₂ (b) Co₃O₄/TiO₂ (c) 5% Fe₃O₄/Co₃O₄-TiO₂ (d) 5% Fe₃O₄/TiO₂ nanoparticles.

XPS spectrum exhibited peaks at 529.06, 529.22, 529.50, and 529.71 eV assigned to lattice oxygen while the peak at 531.5 eV assigned to oxygen defect sites and surface oxygen [24,66,70].

3.5. UV-vis spectroscopy

Figure 5 shows the optical absorption spectra of TiO₂, Co₃O₄-TiO₂, Fe₃O₄/TiO₂ and Fe₃O₄/Co₃O₄-TiO₂ nanoparticles. Undoped TiO₂ displayed an absorbance just below 410 nm resulted due to its band gap excitation [23]. The spectra of the doped TiO₂ samples showed a redshift of absorption edge to higher wavelengths indicate that the addition of Co and Fe ions led to a decrease in the band gap of TiO₂. This resulted due to introduce of additional energy levels in the bandgap of TiO₂ [74]. Also, Fig. 5 showed the intensity of visible-light absorption gradually increased with increasing the Fe₃O₄ amount. Moreover, the doped TiO₂ samples showed new

absorption thresholds appeared at 426 and 526 nm indicating the creation of oxygen vacancies and formation and d-d spin forbidden transition of Co³⁺ and Fe³⁺ [51,75]. Another new absorption bands appeared at 670 and 745 nm may be resulted due to the splitting of electrons states in the d-orbital of Co²⁺, showing the d-d transition, and charge transfer transition from oxygen to Co²⁺ [24,51,55]. These results emphasized the incorporation of Co and Fe ions into the TiO₂ lattice [48,60].

The band gap energy (E_g) of the prepared samples was estimated using Tauc's equation as shown in Fig. S2. The calculated values of E_g are listed in Table 1. Form Table 1, the E_g of TiO₂ reduced sharply after the addition of Co and Fe ions. Furthermore, the E_g of TiO₂ decreased gradually with increasing the Fe₃O₄ amount. The enhancing of visible light absorption and the narrowing of E_g of TiO₂ after the addition of Co and Fe ions could be ascribed to the creation of new energy levels in the band gap of TiO₂ and following the

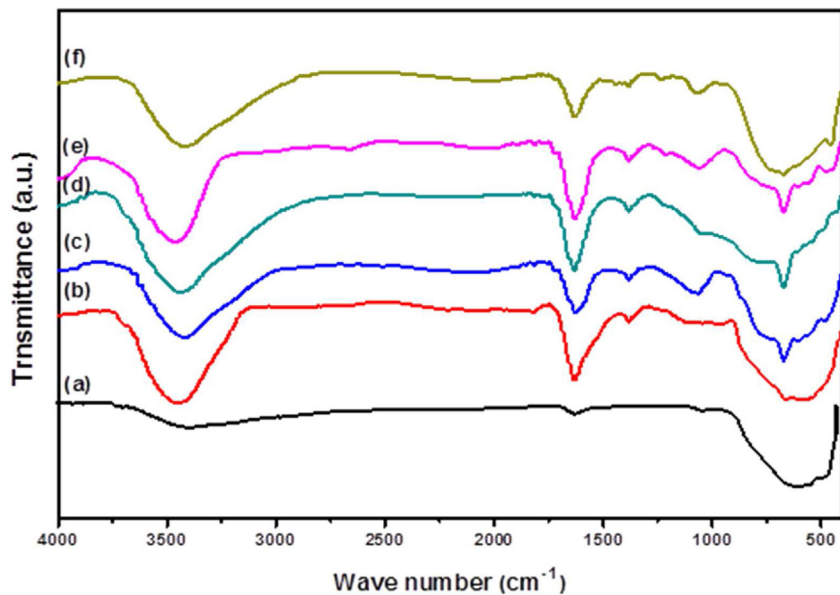


Fig. 3 – FTIR spectra of (a) TiO_2 (b) $\text{Co}_3\text{O}_4/\text{TiO}_2$ (c) 2% $\text{Fe}_3\text{O}_4/\text{Co}_3\text{O}_4-\text{TiO}_2$ (d) 5% $\text{Fe}_3\text{O}_4/\text{Co}_3\text{O}_4-\text{TiO}_2$ (e) 10% $\text{Fe}_3\text{O}_4/\text{Co}_3\text{O}_4-\text{TiO}_2$ (f) 5% $\text{Fe}_3\text{O}_4/\text{TiO}_2$ nanoparticles.

excitation of d-electrons of Co and Fe oxides to the valence or conduction band of TiO_2 or d-d transition among the Fe ions [47,74,76].

It is remarkable to note that, the E_g of 5% $\text{Fe}_3\text{O}_4/\text{Co}_3\text{O}_4-\text{TiO}_2$ is much lower and the absorption in the visible region is much higher than that of the 5% $\text{Fe}_3\text{O}_4/\text{TiO}_2$. This demonstrates that the co-doping of TiO_2 with Co and Fe ions enhanced the separation and inhibited the recombination of photogenerated charges and decreased the band gap width of TiO_2 and consequently, improved the photocatalytic properties of TiO_2 under visible light irradiation [77].

3.6. Photoluminescence (PL)

Photoluminescence (PL) is a suitable technique to investigate the recombination rate of photogenerated $e^- - h^+$ pairs and consequently, knowing extent of the photocatalyst efficiency. The PL emission spectra of pure TiO_2 , $\text{Co}_3\text{O}_4-\text{TiO}_2$, $\text{Fe}_3\text{O}_4/\text{TiO}_2$ and $\text{Fe}_3\text{O}_4/\text{Co}_3\text{O}_4-\text{TiO}_2$ samples were recorded at 325 nm excitation wavelength, as displayed in Fig. 6. The samples displayed three emission peaks appeared at 410, 461 and 520 nm. The emission peak at 410 nm ascribed to the free excitation emission of the band gap [78], while the peaks at 461 and 520 nm are probably arising from the defect centers associated with oxygen vacancies with one and two trapped electrons, respectively [24,78]. As shown in Fig. 6, all of the doped TiO_2 have lower PL intensity compared to pure TiO_2 indicating the role of dopants in inhibition the recombination of $e^- - h^+$ pairs. In addition, the PL intensity suppressed effectively with increasing the Fe_3O_4 amount and 5% $\text{Fe}_3\text{O}_4/\text{Co}_3\text{O}_4-\text{TiO}_2$ showed the lowest PL intensity implying that the 5 wt.% of Fe_3O_4 is an optimal doping amount. In contrast, by increasing the Fe_3O_4 amount to 10 wt.%, the PL intensity increased which demonstrated that the suppression of the recombination depends strongly on the amount of Fe_3O_4 .

For identifying the role of Co ions in the retardation of recombination, the results of PL spectra (Fig. 6) illustrated that the PL intensity of 5% $\text{Fe}_3\text{O}_4/\text{Co}_3\text{O}_4-\text{TiO}_2$ is significantly lower than that of 5% $\text{Fe}_3\text{O}_4/\text{TiO}_2$ which has Fe ions only, indicating the synergistic effect between Co and Fe ions played important role in reducing the recombination $e^- - h^+$ pairs and consequently enhancing the photocatalytic activity of TiO_2 . The role of Co ions in enhancing the separation of $e^- - h^+$ pairs maybe resulted due to the ability of Co ions to trap the conduction electrons of TiO_2 effectively due to its high reduction potential ($\text{Co}^{3+} + e = \text{Co}^{2+}$, $E_0 = +1.81$ V) and can induce p-type conductivity onto the TiO_2 leading formation of p-n junction which facilitated the migration of the holes toward the photocatalyst surface [79].

3.7. Photocatalytic activity measurements

3.7.1. Photodegradation of TC and Pl

The photocatalytic activity of TiO_2 , $\text{Co}_3\text{O}_4-\text{TiO}_2$, $\text{Fe}_3\text{O}_4/\text{Co}_3\text{O}_4-\text{TiO}_2$ and $\text{Fe}_3\text{O}_4/\text{TiO}_2$ nanoparticles were investigated by degradation of TC and Pl under sunlight illumination as shown in Fig. 7. The results showed that the photodegradation of TC and Pl enhanced significantly after the addition of Co and Fe ions to TiO_2 . In addition, Fig. 7 displayed that the photodegradation of both two pollutants increased gradually with increasing the Fe_3O_4 amount and the 5% $\text{Fe}_3\text{O}_4/\text{Co}_3\text{O}_4-\text{TiO}_2$ showed the highest activity with nearly 100% of degradation compared with other contents of Fe_3O_4 . The enhancing in the photodegradation efficiency of TiO_2 after the addition of Co_3O_4 and Fe_3O_4 ascribed to the dual role trappers of Fe^{2+} and Fe^{3+} (Eqs. (1) and (2)) and Co^{2+} and Co^{3+} (Eqs. (4) and (5)) which acted as electrons and holes trappers which in turn firmly inhibited the recombination process of $e^- - h^+$ and extended their lifetimes of $e^- - h^+$ [74,80–82]. However, when the Fe_3O_4 amount exceeded 5 wt.%, the photocatalytic

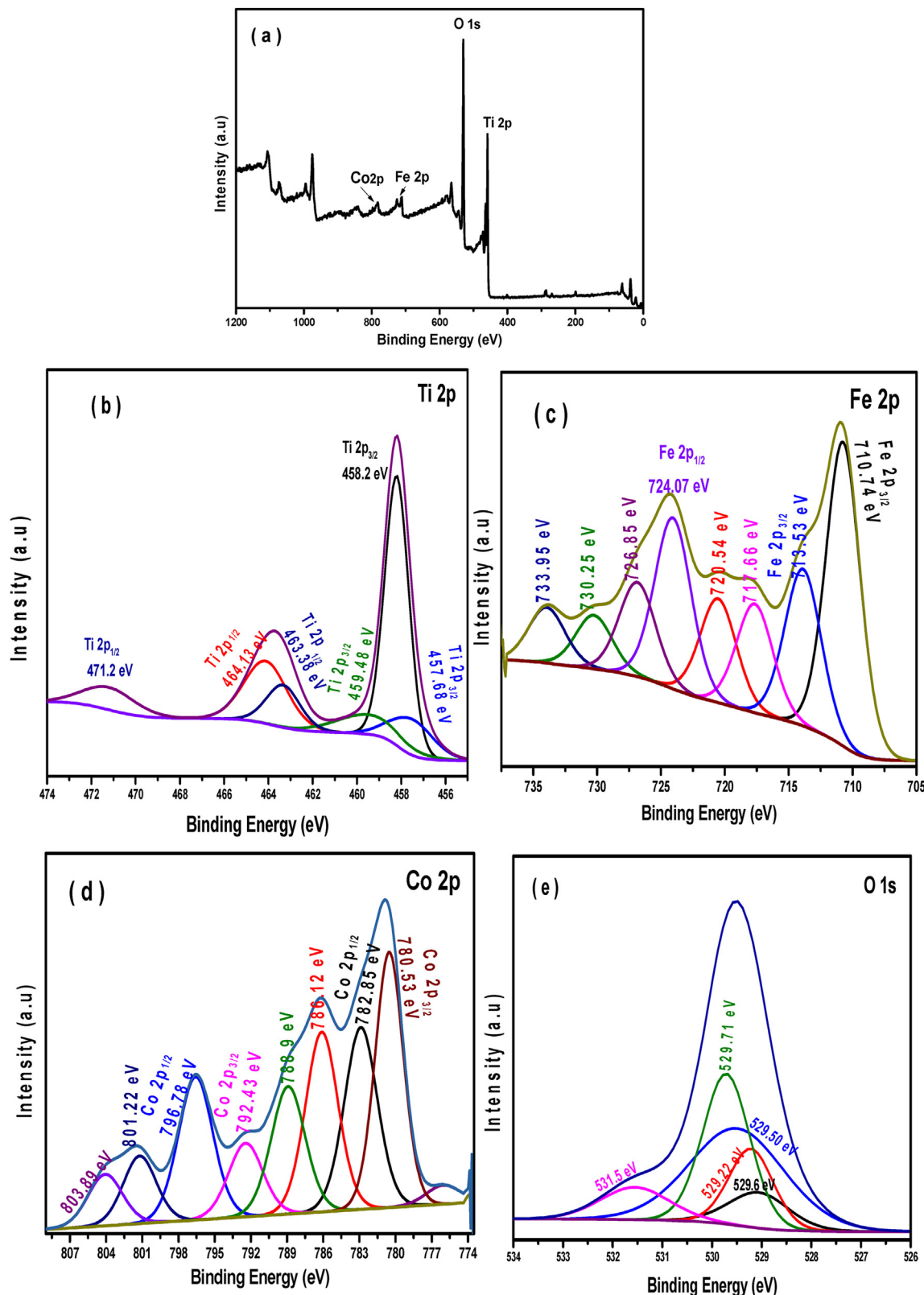


Fig. 4 – XPS results of 5% $\text{Fe}_3\text{O}_4/\text{Co}_3\text{O}_4-\text{TiO}_2$ nanoparticles.

efficiency of $\text{Co}_3\text{O}_4-\text{TiO}_2$ was decreased indicating the Fe^{3+} at higher concentrations acted as a recombination center of photogenerated $e^- - h^+$ pairs [80,83]. Moreover, increasing the Fe_3O_4 amount promoted the aggregation or formation of

multilayers of Fe_3O_4 on the surface of $\text{Co}_3\text{O}_4-\text{TiO}_2$ which in turn shielded the light to arrival into the $\text{Co}_3\text{O}_4-\text{TiO}_2$ surface and consequently, reduced of the number of photogenerated charge carriers [23].

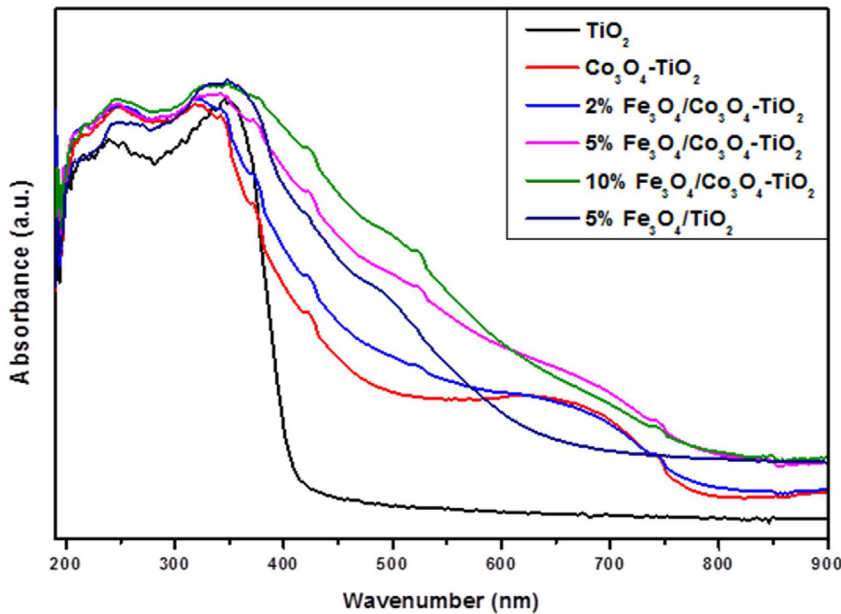
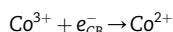
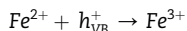
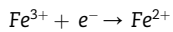


Fig. 5 – UV–vis absorbance spectra of undoped and doped TiO_2 nanoparticles.



For comparison, Fig. 7 showed the photocatalytic activity of 5% $\text{Fe}_3\text{O}_4/\text{Co}_3\text{O}_4\text{-TiO}_2$ is much higher than that of 5% $\text{Fe}_3\text{O}_4/\text{TiO}_2$ (without Co ions) for degradation of TC and Pl. The enhancing in the photocatalytic performance of TiO_2 after

doped with double metal (5% $\text{Fe}_3\text{O}_4/\text{Co}_3\text{O}_4\text{-TiO}_2$) compared with the single doped TiO_2 ($\text{Co}_3\text{O}_4\text{-TiO}_2$ and 5% $\text{Fe}_3\text{O}_4/\text{TiO}_2$) resulted from the synergistic effect between Co and Fe ions which played important role in inhibiting the recombination rate of $e^- - h^+$ pairs which in turn enhanced the photoactivity of TiO_2 . In addition, the existence of anatase and rutile phase together, Ti^{3+} and oxygen vacancies played together in enhancing the photocatalytic activity of TiO_2 [84].

The photodegradation kinetics of TC and Pl were investigated using the Langmuir–Hinshelwood first-order kinetic model according to the following formula [85]: $\ln \left(\frac{C_0}{C_t} \right) = kt$. Fig. S3 showed the kinetic curves of TC and Pl degradation and

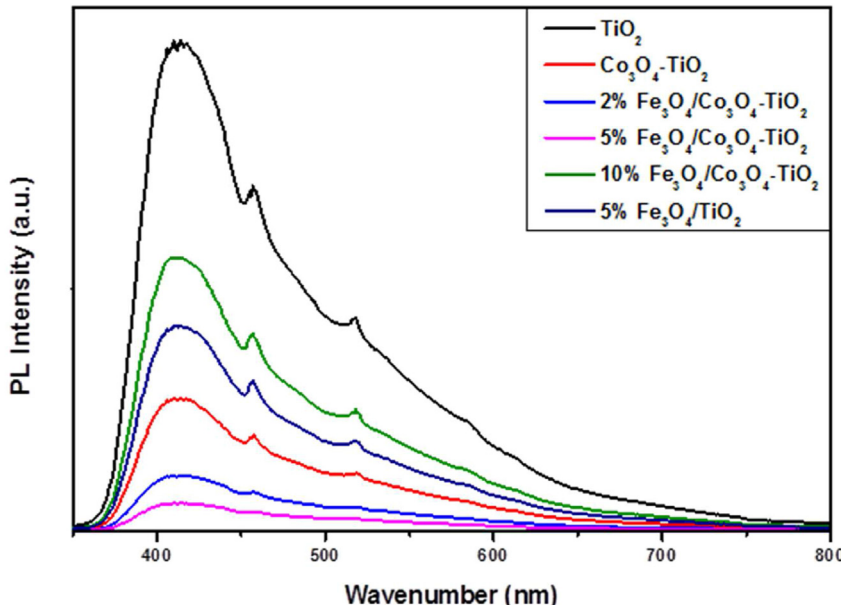


Fig. 6 – Photoluminescence spectra of undoped and doped TiO_2 nanoparticles.

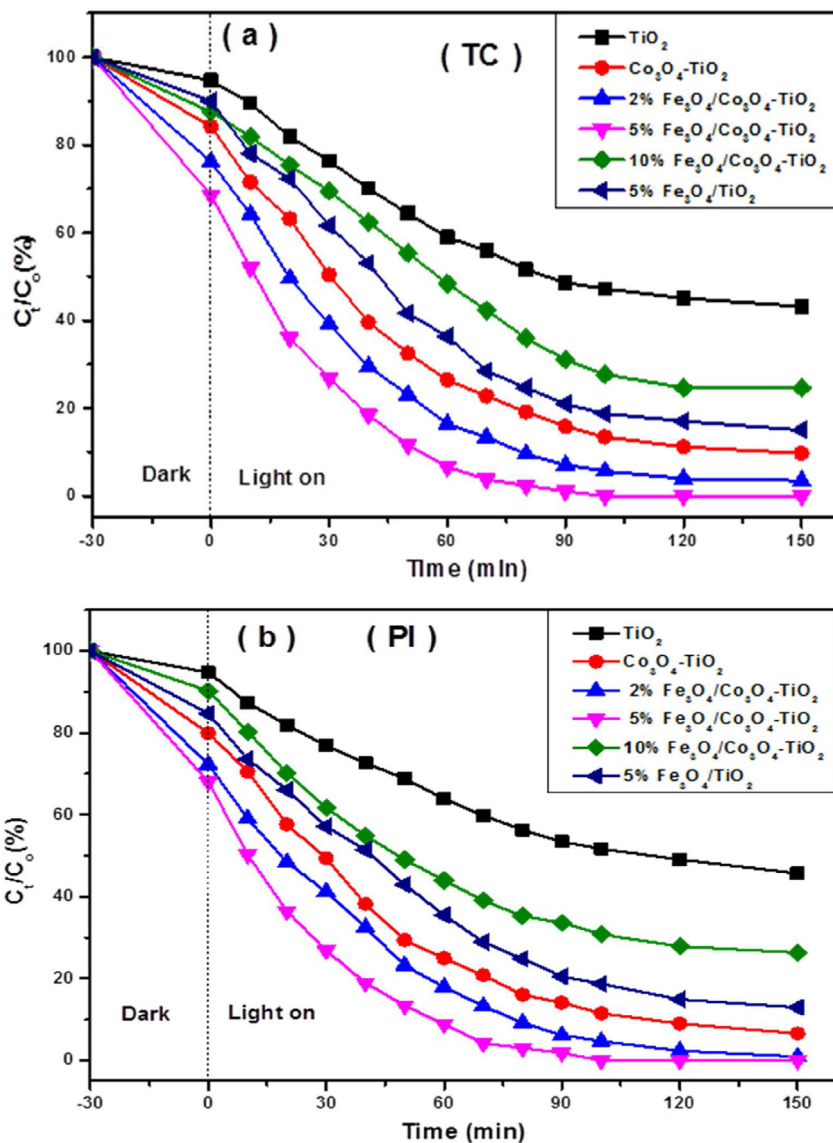


Fig. 7 – Photodegradation efficiency of undoped and doped TiO_2 nanoparticles.

the calculated degradation kinetics parameters were listed in **Table 2**. The results indicated that the photodegradation of TC and Pl follows the pseudo first-order kinetics. Also, **Table 2** displays that the photodegradation rate k increased with

increasing Fe_3O_4 amount and the 5% $\text{Fe}_3\text{O}_4/\text{Co}_3\text{O}_4-\text{TiO}_2$ showed the highest photodegradation rate.

The mineralization of TC and Pl was evaluated by TOC analysis at different intervals of irradiation time over 5% $\text{Fe}_3\text{O}_4/\text{Co}_3\text{O}_4-\text{TiO}_2$ as shown in **Fig. S4**. After 100 min, the degradation results were 100% of both TC and Pl while the % TOC removal efficiencies for TC and Pl were 67.4% and 85.6%, respectively after 180 min. However, increasing the irradiation time to 240 min, the %TOC reached 100% for TC and Pl indicating the complete mineralization of TC and Pl into CO_2 and H_2O . The results above demonstrate that the 5% $\text{Fe}_3\text{O}_4/\text{Co}_3\text{O}_4-\text{TiO}_2$ showed the highest photocatalytic activity and both TC and Pl can be mineralized effectively and completely.

To compare the photocatalytic performance of our samples with other photocatalysts, **Table 1S** shows that the 5% $\text{Fe}_3\text{O}_4/\text{Co}_3\text{O}_4-\text{TiO}_2$ showed excellent photocatalytic performance compared with other literatures for photodegradation

Table 2 – Correlation coefficients and rate constants for TC and Pl photodegradation.

Samples	TC		Phenol	
	$K (\text{min}^{-1})$	R^2	$K (\text{min}^{-1})$	R^2
TiO_2	0.007	0.99552	0.0064	0.99964
2% $\text{Co}_3\text{O}_4-\text{TiO}_2$	0.01794	0.99571	0.01975	0.99829
2% $\text{Fe}_3\text{O}_4/\text{Co}_3\text{O}_4-\text{TiO}_2$	0.02407	0.99905	0.02498	0.99627
5% $\text{Fe}_3\text{O}_4/\text{Co}_3\text{O}_4-\text{TiO}_2$	0.03447	0.9984	0.03652	0.9939
10% $\text{Fe}_3\text{O}_4/\text{Co}_3\text{O}_4-\text{TiO}_2$	0.0096	0.99698	0.01174	0.99969
5% $\text{Fe}_3\text{O}_4/\text{TiO}_2$	0.01311	0.98837	0.01487	0.99704

of organic pollutants and for H₂ production under sunlight illumination [13,86–89].

3.7.2. Hydrogen production

Figure 8 shows that the photocatalytic performance of pure and doped TiO₂ was enhanced significantly after doping of TiO₂ with Co and Fe ions. No appreciable H₂ was detected in case of pure TiO₂ while the 5%Fe₃O₄/TiO₂ gave very small amount of H₂ compared with 5%Fe₃O₄/Co₃O₄–TiO₂ after 5 h. On the other hand, the 5%Fe₃O₄/Co₃O₄–TiO₂ showed the highest activity towards H₂ production compared with other content of Fe₃O₄ with 2890 μmol g⁻¹. **Fig. S5** showed the effect of sacrificial agent on the mount of H₂ production where the amount of generated H₂ increased after the addition of sacrificial agent compared with that without using sacrificial agent. Based on these results, the synergistic effect between Co and Fe ions enhanced the photocatalytic activity of TiO₂ significantly.

3.7.2.1. Photocatalytic mechanism. To understand the role of active radicals in the photodegradation of TC and Pl over 5% Fe₃O₄/Co₃O₄–TiO₂ nanoparticles, different scavengers were used as shown in **Fig. S6**. Based on the results, the photodegradation of both TC and Pl are greatly suppressed after the addition of IPA and BQ scavengers where the photodegradation efficiencies were 15.8% and 22.5% of TC and 31.4% and 25.3% of Pl after 1 h, respectively. On the other hand, the addition of Na₂EDTA (h⁺ scavenger) was accompanied by slight retardation with 50.2% and 59.8% for TC and Pl, respectively, after 1 h of photoreaction. According to these results, •O₂⁻ and •OH species are the primary active species in the photodegradation of TC and Pl while h⁺ played a less important role.

In addition, the active species in photocatalysts was determined using electron spin resonance (ESR). As displayed

in **Fig. S7**, no noticeable signals of both DMPO–•O₂⁻ and DMPO–•OH adducts were detected in the 5% Fe₃O₄/Co₃O₄–TiO₂ nanoparticles under dark condition. However, under sunlight illumination, quadruple signal with an intensity ratio of 1:2:2:1 for DMPO–•OH adduct is detected indicating that •OH radicals were generated during the photocatalytic reaction (**Fig. S7**). Similarly, the spectrum of DMPO–•O₂⁻ showed four characteristic peaks with intensity ratio of 1:1:1:1 under sunlight illumination. According to these results, •O₂⁻ and •OH are the active species in the photodegradation of PI and TC.

The work function of the TiO₂, Fe₃O₄ and Co₃O₄ were determined using ultraviolet photoelectron spectroscopy (UPS) as shown in **Fig. S8**. The work function was determined by the following equation: $\Phi = h\nu - E_{\text{cutoff}}$, where Φ , $h\nu$, and E_{cutoff} are the work function, incoming photon energy from the He I source (21.21 eV), and the secondary electron cutoff energy, respectively. The calculated work function for the TiO₂, Fe₃O₄ and Co₃O₄ are 5.67, 5.20 and 5.17 eV which indicates that the TiO₂ has the highest work function compared with Fe₃O₄ and Co₃O₄.

On the basis of these results above, the mechanism of the photodegradation of TC and Pl under sunlight irradiation is proposed according of S-scheme heterojunction as shown in **Scheme 1** [27,28,30]. Ternary heterojunction was formed when Fe₃O₄ and Co₃O₄ entities were put into contact with TiO₂, electron transfer occurred at the interface from Fe₃O₄ and Co₃O₄ to TiO₂, because the work function of TiO₂ is larger than that of Fe₃O₄ and Co₃O₄, leading formation of electron depletion layer near the interface of Fe₃O₄ and Co₃O₄ and electrons accumulation layer in the TiO₂ [30]. Under sunlight illumination, the photogenerated electrons in the CB of TiO₂ recombined with the photogenerated holes in the VB of Fe₃O₄ and Co₃O₄ driven by the internal electric field, which in turn prevented the recombination of the powerful photogenerated electrons in CB of Fe₃O₄ and Co₃O₄ and the photogenerated

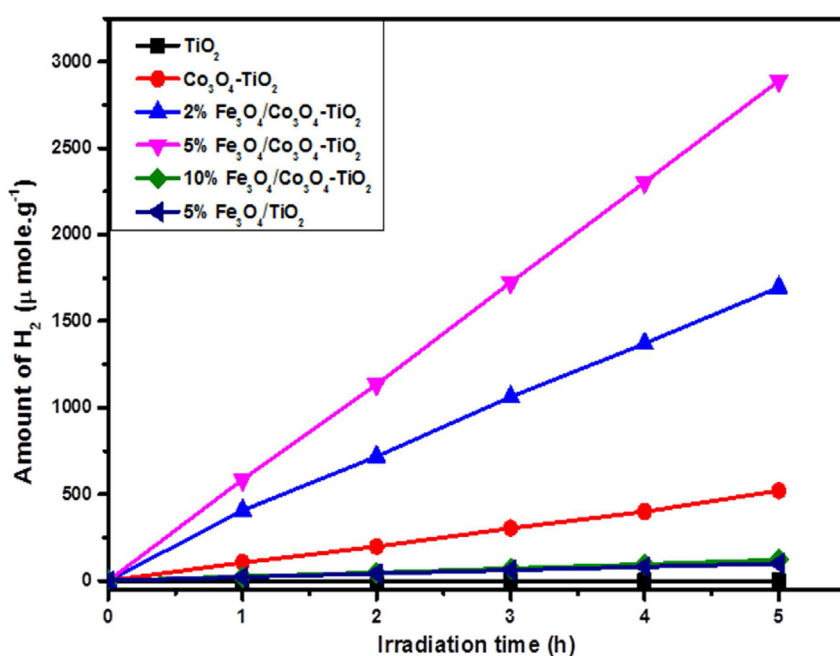
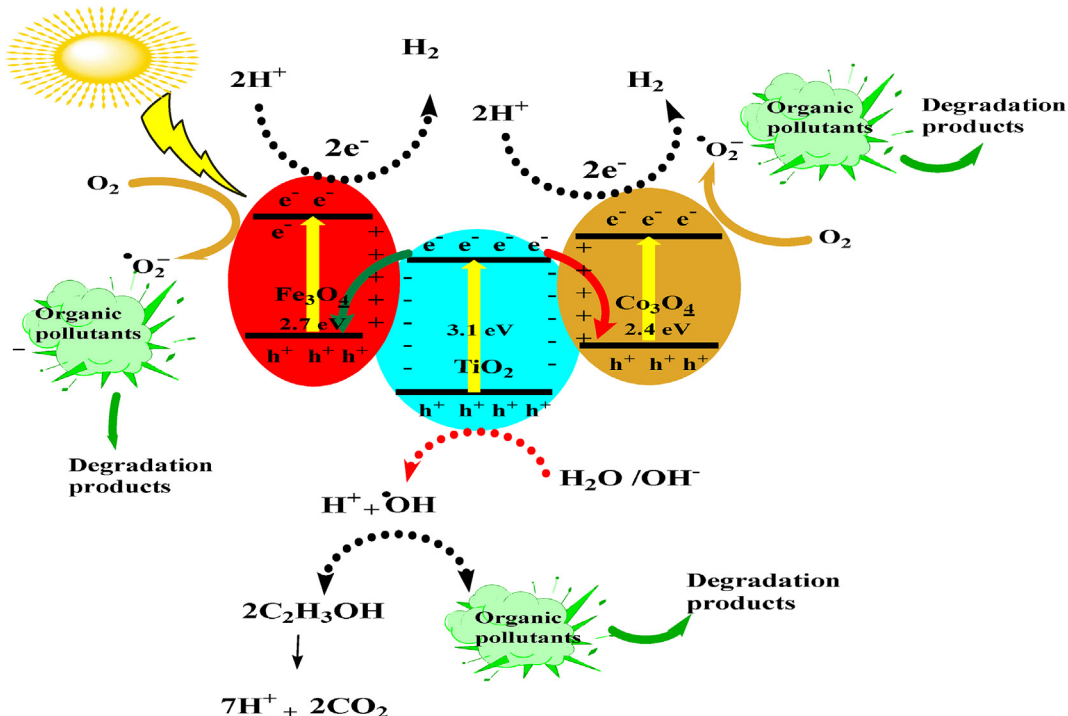
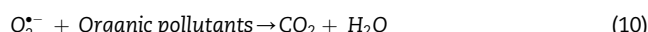
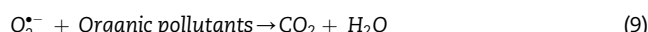


Fig. 8 – Photocatalytic activity for H₂ production over undoped and doped TiO₂.



Scheme 1 – Postulated mechanism of electrons and holes transfer in $\text{Fe}_3\text{O}_4/\text{Co}_3\text{O}_4-\text{TiO}_2$ nanoparticles.

holes in VB of TiO_2 leading enhancing the photodegradation of PL and TC and for H_2 production [90]. The photogenerated electrons in CB of Fe_3O_4 and Co_3O_4 react with oxygen molecules on the surface of photocatalysts to generate superoxide radical $\cdot\text{O}_2^-$ (Eqs. (6) and (7)), while the photogenerated holes react with hydroxyl groups and water molecules on the surface of catalyst to produced $\cdot\text{OH}$ radicals (Eq. (8)) [47,83], and these electrons and holes migrate to the surface of photocatalyst to initiate the photodegradation of TC and PI (Eqs. (9) and (10)) [87]. The mechanism of H_2 evolution also is displayed in Scheme 1. In this mechanism, the photogenerated holes reacted with H_2O and produced $\cdot\text{OH}$ and H^+ (Eq. (8)). The resulted $\cdot\text{OH}$ radicals attract the sacrificial agent molecules (ethanol) and produced H^+ (Eq. (11)). The resulted H^+ ions were reduced by the photogenerated electrons and finally resulted H_2 (Eq. (12)).



3.7.3. Reusability study

The reusability and stability of the prepared samples were investigated. The repetitive experiments were carried out under the same experimental conductions. After each cycle, the catalyst was separated and washed with distilled water several times and then ethanol and finally dried at 100 °C for 8 h. Fig. S9 show the photodegradation results of TC and PI over 5% $\text{Fe}_3\text{O}_4/\text{Co}_3\text{O}_4-\text{TiO}_2$ after five cycles. Slight decrease in the photocatalytic activity was observed after five cycles, indicating the stability of $\text{Fe}_3\text{O}_4/\text{Co}_3\text{O}_4-\text{TiO}_2$ nanoparticles. The sample that used for investigation the reusability (5% $\text{Fe}_3\text{O}_4/\text{Co}_3\text{O}_4-\text{TiO}_2$) was characterized by XRD and TEM analysis before and after five cycles to investigate the effect of reused times on the photocatalyst structure. Fig. S10 showed no changes in the structure and morphology of photocatalyst after five cycles compared with fresh sample, indicating the high stability of prepared photocatalyst. Based on these results, the photocatalyst displayed high stability and can be reused several times in photocatalytic reactions without significant changes in its structure which makes these photocatalysts applicable materials for treatment of waste water and for H_2 production.

4. Conclusion

New ternary heterojunction $\text{Fe}_3\text{O}_4/\text{Co}_3\text{O}_4-\text{TiO}_2$ with S-scheme mechanism under solar-light-driven were prepared successfully via sol-gel method. The obtained XRD results showed no phase change of TiO_2 was observed after the addition of Co^{n+}

and Fe^{n+} ions. DRS results displayed that the absorption of visible light was enhanced significantly after doping TiO_2 by Co^n and Fe^{n+} and the E_g was reduced sharply from 3.10 to 1.72 eV. XPS results emphasized the existence of multivalent states of Fe and Co ions (Co^{2+} , Co^{3+} , Fe^{2+} and Fe^{3+}) which played important role in inhibition the recombination of $e^- - h^+$ as illustrated from PL results and enhanced the photocatalytic activity of TiO_2 . The photodegradation of TC and Pl and for H_2 production enhanced significantly after doped TiO_2 by Co^{n+} and Fe^{n+} together compared with pure mono-doped samples. %TOC results emphasized the complete degradation of TC and Pl to CO_2 and H_2O and the degradation kinetics obeyed the pseudo-first order. The scavenging results showed that the $\cdot\text{OH}$ and $\cdot\text{O}_2^-$ radicals were the active species for degradation of TC and Pl. The formation of ternary heterojunction enhanced the sunlight absorption, prevent the recombination of photogenerated charges and enhanced the photocatalytic performance greatly.

Declaration of Competing Interest

The authors declare that they have no known competing financial interests or personal relationships that could have appeared to influence the work reported in this paper.

Acknowledgments

"This work was funded by the University of Jeddah, Jeddah, Saudi Arabia, under grant No. (UJ-21-ICI-11). The authors, therefore, acknowledge with thanks the University of Jeddah technical and financial support".

Appendix A. Supplementary data

Supplementary data to this article can be found online at <https://doi.org/10.1016/j.jmrt.2022.07.078>.

REFERENCES

- [1] Zhao X, Xie W, Deng Z, Wang G, Cao A, Chen H, et al. Salt templated synthesis of NiO/TiO_2 supported carbon nanosheets for photocatalytic hydrogen production. *Colloids Surf A Physicochem Eng Asp* 2020;587:124365.
- [2] Hassan SMH, Mannaa MA, Ibrahim AA. Nano-sized mesoporous phosphated tin oxide as an efficient solid acid catalyst. *RSC Adv* 2019;9:810–8.
- [3] Hezma AM, Rajeh A, Mannaa MA. An insight into the effect of zinc oxide nanoparticles on the structural, thermal, mechanical properties and antimicrobial activity of Cs/PVA composite. *Colloids Surf A Physicochem Eng Asp* 2019;581:123821.
- [4] Ibrahim AA, Hassan SM, Mannaa MA. Mesoporous tin oxide-supported phosphomolybdic acid as high performance acid catalysts for the synthesis of hydroquinone diacetate. *Colloids Surf A Physicochem Eng Asp* 2020;586:124248.
- [5] Mannaa MA, Altass HM, Salama RS. MCM-41 grafted with citric acid: the role of carboxylic groups in enhancing the synthesis of xanthenes and removal of heavy metal ions. *Environ Nanotechnol Monit Manag* 2021;15:100410.
- [6] Salama RS, El-Bahy SM, Mannaa MA. Sulfamic acid supported on mesoporous MCM-41 as a novel, efficient and reusable heterogenous solid acid catalyst for synthesis of xanthene, dihydropyrimidinone and coumarin derivatives. *Colloids Surf A Physicochem Eng Asp* 2021;628:127261.
- [7] Tang L, Liu L, Yang F. FeMoO_4 -graphene oxide photo-electrocatalyst for berberine removal and hydrogen evolution. *Int J Hydrogen Energy* 2019;44:19755–61.
- [8] Alsulami QA, Rajeh A, Mannaa MA, Albukhari SM, Baamer DF. Preparation of highly efficient sunlight driven photodegradation of some organic pollutants and H_2 evolution over rGO/FeVO_4 nanocomposites. *Int J Hydrogen Energy* 2021;46:27349–63.
- [9] Sun T, Fan J, Liu E, Liu L, Wang Y, Dai H, et al. Fe and Ni co-doped TiO_2 nanoparticles prepared by alcohol-thermal method: application in hydrogen evolution by water splitting under visible light irradiation. *Powder Technol* 2012;228:210–8.
- [10] Alsulami QA, Rajeh A, Mannaa MA, Albukhari SM, Baamer DF. One-step preparation of $\text{RGO}/\text{Fe}_3\text{O}_4-\text{FeVO}_4$ nanocomposites as highly effective photocatalysts under natural sunlight illumination. *Sci Rep* 2022;12:1–12.
- [11] Radecka M, Wnuk A, Trenczek-Zajac A, Schneider K, Zakrzewska K. $\text{TiO}_2/\text{SnO}_2$ nanotubes for hydrogen generation by photoelectrochemical water splitting. *Int J Hydrogen Energy* 2015;40:841–51.
- [12] Hassan SM, Ahmed AI, Mannaa MA. Surface acidity, catalytic and photocatalytic activities of new type $\text{H}_3\text{PW}_{12}\text{O}_{40}/\text{Sn-TiO}_2$ nanoparticles. *Colloids Surf A Physicochem Eng Asp* 2019;577:147–57.
- [13] Craciun E, Preoana L, Atkinson I, Jitaru I, Anghel EM, Bratan V, et al. Fe^{3+} -doped TiO_2 nanopowders for photocatalytic mineralization of oxalic acid under solar light irradiation. *J Photochem Photobiol Chem* 2018;356:18–28.
- [14] Velázquez-Martínez S, Silva-Martínez S, Pineda-Arellano CA, Jiménez-González A, Salgado-Tránsito I, Morales-Pérez AA, et al. Modified sol-gel/hydrothermal method for the synthesis of microsized TiO_2 and iron-doped TiO_2 , its characterization and solar photocatalytic activity for an azo dye degradation. *J Photochem Photobiol Chem* 2018;359:93–101.
- [15] Alshorifi FT, Alswat AA, Mannaa MA, Alotaibi MT, El-Bahy SM, Salama RS. Facile and green synthesis of silver quantum dots immobilized onto a polymeric CTS-PEO blend for the photocatalytic degradation of p-nitrophenol. *ACS Omega* 2021;6:30432–41.
- [16] Li H, Ren F, Li Q, Yang J, Wang Y, Cheng Z. Spin-flip effect enhanced photocatalytic activity in Fe and single-electron-trapped oxygen vacancy co-doped TiO_2 . *Appl Surf Sci* 2018;457:633–43.
- [17] Yang G, Jiang Z, Shi H, Xiao T, Yan Z. Preparation of highly visible-light active N-doped TiO_2 photocatalyst. *J Mater Chem* 2010;20:5301–9.
- [18] Yang G, Xiao T, Sloan J, Li G, Yan Z. Lowerature synthesis of visible-light active fluorine/sulfur co-doped mesoporous TiO_2 microspheres. *Chem Eur J* 2011;17:1096–100.
- [19] Sun M, Fang Y, Kong Y, Yuan X, Shi J, Umar A. Direct in situ synthesis of Fe_2O_3 -codoped N-doped TiO_2 nanoparticles with enhanced photocatalytic and photo-electrochemical properties. *J Alloys Compd* 2017;705:89–97.
- [20] Shi H, Zhou M, Song D, Pan X, Fu J, Zhou J, et al. Highly porous $\text{SnO}_2/\text{TiO}_2$ electrospun nanofibers with high photocatalytic activities. *Ceram Int* 2014;40:10383–93.
- [21] Yang G, Yan Z, Xiao T. Preparation and characterization of $\text{SnO}_2/\text{ZnO}/\text{TiO}_2$ composite semiconductor with enhanced photocatalytic activity. *Appl Surf Sci* 2012;258:8704–12.

- [22] Niu J, Yao B, Chen Y, Peng C, Yu X, Zhang J, et al. Enhanced photocatalytic activity of nitrogen doped TiO_2 photocatalysts sensitized by metallo Co, Ni-porphyrins. *Appl Surf Sci* 2013;271:39–44.
- [23] Hassan SM, Ahmed AI, Manna MA. Structural, photocatalytic, biological and catalytic properties of $\text{SnO}_2/\text{TiO}_2$ nanoparticles. *Ceram Int* 2018;44:6201–11.
- [24] Jaihind DP, Verma A, Chen CC, Huang YC, Dong CL, Fu YP. Study of oxidation states of Fe- and Co-doped TiO_2 photocatalytic energy materials and their visible-light-driven photocatalytic behavior. *Int J Hydrogen Energy* 2019;44:15892–906.
- [25] Ge H, Xu F, Cheng B, Yu J, Ho W. S-scheme heterojunction TiO_2/CdS nanocomposite nanofiber as H_2 -production photocatalyst. *ChemCatChem* 2019;11:6301–9.
- [26] Enesca A, Andronic L. Photocatalytic activity of S-scheme heterostructure for hydrogen production and organic pollutant removal: a mini-review. *Nanomaterials* 2021;11:871.
- [27] Zhang L, Zhang J, Yu H, Yu J. Emerging S-scheme photocatalyst. *Adv Mater* 2022;34:2107668.
- [28] Xu Q, Wageh S, Al-Ghamdi AA, Li X. Design principle of S-scheme heterojunction photocatalyst. *J Mater Sci Technol* 2022;124:171–3.
- [29] Fazli A, Brigante M, Khataee A, Mailhot G. Synthesis of a magnetically separable LDH-based S-scheme nano-heterojunction for the activation of peroxyomonosulfate towards the efficient visible-light photodegradation of diethyl phthalate. *Appl Surf Sci* 2021;559:149906.
- [30] Xu Q, Zhang L, Cheng B, Fan J, Yu J. S-scheme heterojunction photocatalyst. *Chem* 2020;6:1543–59.
- [31] Zhang L, Li Y, Zhang Q, Wang H. Well-dispersed Pt nanocrystals on the heterostructured $\text{TiO}_2/\text{SnO}_2$ nanofibers and the enhanced photocatalytic properties. *Appl. Surf Sci* 2014;319:21–8.
- [32] Asuha S, Zhou XG, Zhao S. Adsorption of methyl orange and Cr(VI) on mesoporous TiO_2 prepared by hydrothermal method. *J Hazard Mater* 2010;181:204–10.
- [33] Kongsong P, Sikong L, Niyomwas S, Rachpech V. Photocatalytic antibacterial performance of glass fibers thin film coated with N-doped $\text{SnO}_2/\text{TiO}_2$. *Sci World J* 2014;2014:1–9.
- [34] Pei Z, Kaiqiang Z, Yu D, Bo B, Weisheng G, Yourui S. Adsorption of organic dyes by $\text{TiO}_2@\text{Yeast}$ -carbon composite microspheres and their in situ regeneration evaluation. *J Nanomater* 2015;2015:1–13. <https://doi.org/10.1155/2015/498304>.
- [35] Salama RS, Hassan SM, Ahmed AI, El-Yazeed WSA, Manna MA. The role of PMA in enhancing the surface acidity and catalytic activity of a bimetallic Cr-Mg-MOF and its applications for synthesis of coumarin and dihydropyrimidinone derivatives. *RSC Adv* 2020;10:21115–28.
- [36] Alghamdi HM, Abutalib MM, Rajeh A, Manna MA, Nur O, Abdelrazek EM. Effect of the $\text{Fe}_2\text{O}_3/\text{TiO}_2$ nanoparticles on the structural, mechanical, electrical properties and antibacterial activity of the biodegradable chitosan/polyvinyl alcohol blend for food packaging. *J Polym Environ* 2022;43:22215–25.
- [37] Pouretedal HR, Bashiri Z, Nasiri M, Arab A. Photo-treatment of TNT wastewater in the presence of nanocomposite of $\text{WO}_3/\text{Fe}_3\text{O}_4$, Part. *Sci Technol* 2021;39:971–80.
- [38] Pouretedal HR, Afshari B. Preparation and characterization of Zr and Sn doped TiO_2 nanocomposite and photocatalytic activity in degradation of tetracycline. *Desalination Water Treat* 2016;57:10941–7.
- [39] Pouretedal HR, Sohrabi AM. Photosensitization of TiO_2 by ZnS and bromo thymol blue and its application in photodegradation of para-nitrophenol. *J Iran Chem Soc* 2016;13:73–9.
- [40] Hassan SM, Manna MA. Photocatalytic degradation of brilliant green dye by $\text{SnO}_2/\text{TiO}_2$ nanocatalysts. *Int J Nano Mater Sci* 2016;5:9–19.
- [41] Hassan SM, Ahmed AI, Manna MA. Surface acidity, catalytic and photocatalytic activities of new type $\text{H}_3\text{PW}_{12}\text{O}_{40}/\text{Sn-TiO}_2$ nanoparticles. *Colloids Surf A Physicochem Eng Asp* 2019;577:147–57.
- [42] Hassan SM, Ahmed AI, Manna MA. Preparation and characterization of SnO_2 doped TiO_2 nanoparticles: effect of phase changes on the photocatalytic and catalytic activity. *J Sci Adv Mater Devices* 2019;4:400–12.
- [43] Deshmane VG, Owen SL, Abrokwa RY, Kuila D. Mesoporous nanocrystalline TiO_2 supported metal (Cu, Co, Ni, Pd, Zn, and Sn) catalysts: effect of metal-support interactions on steam reforming of methanol. *J Mol Catal Chem* 2015;408:202–13.
- [44] Nirmala R, Kim HY, Navamathavan R, Yi C, Won JJ, Jeon K, et al. Photocatalytic activities of electrospun tin oxide doped titanium dioxide nanofibers. *Ceram Int* 2012;38:4533–40.
- [45] Taherinia M, Nasiri M, Abedini E, Pouretedal HR. Influence of calcination temperature and solvent of titanium precursor on the photocatalytic activity of N-doped TiO_2 nanoparticles in H_2 evolution under visible radiation. *Environ Dev Sustain* 2019;21:1963–75.
- [46] Isari AA, Payan A, Fattah M, Jorfi S, Kakavandi B. Photocatalytic degradation of rhodamine B and real textile wastewater using Fe-doped TiO_2 anchored on reduced graphene oxide ($\text{Fe-TiO}_2/\text{rGO}$): characterization and feasibility, mechanism and pathway studies. *Appl Surf Sci* 2018;462:549–64.
- [47] Kalantari K, Kalbasi M, Sohrabi M, Royae SJ. Enhancing the photocatalytic oxidation of dibenzothiophene using visible light responsive Fe and N co-doped TiO_2 nanoparticles. *Ceram Int* 2017;43:973–81.
- [48] Li J, Ren D, Wu Z, Xu J, Bao Y, He S, et al. Flame retardant and visible light-activated Fe-doped TiO_2 thin films anchored to wood surfaces for the photocatalytic degradation of gaseous formaldehyde. *J Colloid Interface Sci* 2018;530:78–87.
- [49] Gnanasekaran L, Hemamalini R, Rajendran S, Qin J, Yola ML, Atar N, et al. Nanosized Fe_3O_4 incorporated on a TiO_2 surface for the enhanced photocatalytic degradation of organic pollutants. *J Mol Liq* 2019;287:110967.
- [50] Mufti N, Munfarriha U, Fuad A, Diantoro M. Synthesis and photocatalytic properties of $\text{Fe}_3\text{O}_4@\text{TiO}_2$ core-shell for degradation of Rhodamine B. *AIP Conf Proc* 2016;1712:050009.
- [51] Suresh R, Giribabu K, Manigandan R, Mangalaraja RV, Solorza JY, Stephen A, et al. Synthesis of Co^{2+} -doped Fe_2O_3 photocatalyst for degradation of pararosaniline dye. *Solid State Sci* 2017;68:39–46.
- [52] Waseem S, Anjum S, Mustafa L, Zeeshan T, Kayani ZN, Javed K. Structural, magnetic and optical investigations of Fe and Ni co-doped TiO_2 dilute magnetic semiconductors. *Ceram Int* 2018;44:17767–74.
- [53] Bian L, Nie J, Jiang X, Song M, Dong F, Shang L, et al. Selective adsorption of uranyl and potentially toxic metal ions at the core-shell $\text{MFe}_2\text{O}_4-\text{TiO}_2$ ($\text{M} = \text{Mn, Fe, Zn, Co, or Ni}$) nanoparticles. *J Hazard Mater* 2019;365:835–45.
- [54] Ganesh I, Gupta AK, Kumar PP, Chandra Sekhar PS, Radha K, Padmanabham G, et al. Preparation and characterization of Co-doped TiO_2 materials for solar light induced current and photocatalytic applications. *Mater Chem Phys* 2012;135:220–34.
- [55] Salavati-Niasari M, Khansari A. Synthesis and characterization of Co_3O_4 nanoparticles by a simple method. *C R Chem* 2014;17:352–8.

- [56] Ma J, Zhang S, Liu W, Zhao Y. Facile preparation of Co_3O_4 nanocrystals via a solvothermal process directly from common Co_2O_3 powder. *J Alloys Compd* 2010;490:647–51.
- [57] Dvořáková M, Perekrestov R, Kšírová P, Balabánová J, Jirátová K, Maixner J, et al. Preparation of cobalt oxide catalysts on stainless steel wire mesh by combination of magnetron sputtering and electrochemical deposition. *Catal Today* 2019;334:13–23.
- [58] Palanisamy B, Babu CM, Sundaravel B, Anandan S, Murugesan V. Sol-gel synthesis of mesoporous mixed $\text{Fe}_2\text{O}_3/\text{TiO}_2$ photocatalyst: application for degradation of 4-chlorophenol. *J Hazard Mater* 2013;252–253:233–42.
- [59] Maji SK, Mukherjee N, Mondal A, Adhikary B. Synthesis, characterization and photocatalytic activity of $\alpha\text{-Fe}_2\text{O}_3$ nanoparticles. *Polyhedron* 2012;33:145–9.
- [60] El Mragui A, Zegaoui O, Daou I. Synthesis, characterization and photocatalytic properties under visible light of doped and co-doped TiO_2 -based nanoparticles. *Mater Today Proc* 2019;13:857–65.
- [61] Çağlar Yılmaz H, Akgeyik E, Bougarrani S, El Azzouzi M, Erdemoğlu S. Photocatalytic degradation of amoxicillin using Co-doped TiO_2 synthesized by reflux method and monitoring of degradation products by LC–MS/MS. *J Dispersion Sci Technol* 2020;41:414–25.
- [62] Wang F, Shen B, Zhu S, Wang Z. Promotion of Fe and Co doped Mn-Ce/ TiO_2 catalysts for low temperature NH₃-SCR with SO₂ tolerance. *Fuel* 2019;249:54–60.
- [63] Tseng HH, Wei MC, Hsiung SF, Chiou CW. Degradation of xylene vapor over Ni-doped TiO_2 photocatalysts prepared by polyol-mediated synthesis. *Chem Eng J* 2009;150:160–7.
- [64] Dong Z, Ding D, Li T, Ning C. Ni-doped TiO_2 nanotubes photoanode for enhanced photoelectrochemical water splitting. *Appl Surf Sci* 2018;443:321–8.
- [65] Liu Q, Ding D, Ning C, Wang X. Black Ni-doped TiO_2 photoanodes for high-efficiency photoelectrochemical water-splitting. *Int J Hydrogen Energy* 2015;40:2107–14.
- [66] Tian L, Xing L, Shen X, Li Q, Ge S, Liu B, et al. Visible light enhanced Fe–I– TiO_2 photocatalysts for the degradation of gaseous benzene. *Atmos Pollut Res* 2020;11:179–85.
- [67] Nanda Gopala Krishna D, George RP, Philip J. Role of oxygen vacancy formation energy and insulating behavior in darkening of white amorphous TiO_2 . *J Phys Chem C* 2021;125:16136–46.
- [68] Cai C, Zhang Z, Liu J, Shan N, Zhang H, Dionysiou DD. Visible light-assisted heterogeneous Fenton with ZnFe_2O_4 for the degradation of Orange II in water. *Appl Catal B Environ* 2016;182:456–68.
- [69] Wang X, nan Zhou Y, Li R, Wang L, Tao L, Ning P. Removal of Hg 0 from a simulated flue gas by photocatalytic oxidation on Fe and Ce co-doped TiO_2 under low temperature. *Chem Eng J* 2019;360:1530–41.
- [70] Wang Z, Hong P, Peng S, Zou T, Yang Y, Xing X, et al. $\text{Co(OH)}_2 @\text{FeCo}_2\text{O}_4$ as electrode material for high performance faradaic supercapacitor application. *Electrochim Acta* 2019;299:312–9.
- [71] Wang X, Zhao SX, Dong L, Lu QL, Zhu J, Nan CW. One-step synthesis of surface-enriched nickel cobalt sulfide nanoparticles on graphene for high-performance supercapacitors. *Energy Storage Mater* 2017;6:180–7.
- [72] Shen B, Zhu S, Zhang X, Chi G, Patel D, Si M, et al. Simultaneous removal of NO and Hg0 using Fe and Co co-doped Mn-Ce/ TiO_2 catalysts. *Fuel* 2018;224:241–9 [d].
- [73] Haw C, Chiu W, Abdul Rahman S, Khiew P, Radiman S, Abdul Shukor R, et al. The design of new magnetic-photocatalyst nanocomposites ($\text{CoFe}_2\text{O}_4\text{-TiO}_2$) as smart nanomaterials for recyclable-photocatalysis applications. *New J Chem* 2016;40:1124–36.
- [74] Gaikwad PN, Hankare PP, Wandre TM, Garadkar KM, Sasikala R. Photocatalytic performance of magnetically separable Fe, N co-doped TiO_2 -cobalt ferrite nanocomposite. *Mater Sci Eng B Solid-State Mater Adv Technol* 2016;205:40–5.
- [75] Liu WX, Ma J, Qu XG, Bin Cao W. Hydrothermal synthesis of (Fe, N) co-doped TiO_2 powders and their photocatalytic properties under visible light irradiation. *Res Chem Intermed* 2009;35:321–8.
- [76] Eshaghi A, Moradi H. Optical and photocatalytic properties of the Fe-doped TiO_2 nanoparticles loaded on the activated carbon. *Adv Powder Technol* 2018;29:1879–85.
- [77] Wang X, nan Zhou Y, Li R, Wang L, Tao L, Ning P. Removal of Hg 0 from a simulated flue gas by photocatalytic oxidation on Fe and Ce co-doped TiO_2 under low temperature. *Chem Eng J* 2019;360:1530–41. <https://doi.org/10.1016/j.cej.2018.10.237>.
- [78] El Mragui A, Logvina Y, da Silva Luís Pinto, Zegaoui O, da Silva JC GE. Synthesis of fe-and co-doped TiO_2 with improved photocatalytic activity under visible irradiation toward carbamazepine degradation. *Materials* 2019;12:4–6.
- [79] Hamal DB, Klabunde KJ. Valence state and catalytic role of cobalt ions in cobalt TiO_2 nanoparticle photocatalysts for acetaldehyde degradation under visible light. *J Phys Chem C* 2011;115:17359–67.
- [80] Delekar SD, Yadav HM, Achary SN, Meena SS, Pawar SH. Structural refinement and photocatalytic activity of Fe-doped anatase TiO_2 nanoparticles. *Appl Surf Sci* 2012;263:536–45.
- [81] Noor S, Sajjad S, Leghari SAK, Flox C, Kallio T. Efficient electrochemical hydrogen evolution reaction and solar activity via bi-functional GO/ $\text{Co}_3\text{O}_4\text{-TiO}_2$ nano hybrid structure. *Int J Hydrogen Energy* 2020;45:17410–21.
- [82] Soo CW, Juan JC, Lai CW, Hamid SBA, Yusop RM. Fe-doped mesoporous anatase-brookite titania in the solar-light-induced photodegradation of Reactive Black 5 dye. *J Taiwan Inst Chem Eng* 2016;68:153–61.
- [83] Wan H, Yao W, Zhu W, Tang Y, Ge H, Shi X, et al. Fe-N co-doped $\text{SiO}_2 @\text{TiO}_2$ yolk-shell hollow nanospheres with enhanced visible light photocatalytic degradation. *Appl Surf Sci* 2018;444:355–63.
- [84] Krishna NG, George RP, Philip J. Anomalous enhancement of corrosion resistance and antibacterial property of commercially pure Titanium (CP-Ti) with nanoscale rutile titania film. *Corros Sci* 2020;172:108678.
- [85] Pouretedal HR, Shevidi O, Nasiri M, Pourhasan FS. Red water treatment by photodegradation process in presence of modified TiO_2 nanoparticles and validation of treatment efficiency by MLR technique. *J Iran Chem Soc* 2016;13:2267–74.
- [86] Anushree C, Nanda Gopala Krishna D, Philip J. Efficient dye degradation via catalytic persulfate activation using iron oxide-manganese oxide core-shell particle doped with transition metal ions. *J Mol Liq* 2021;337:116429.
- [87] Harifi T, Montazer M. $\text{Fe}^{3+}\text{:Ag/TiO}_2$ nanocomposite: synthesis, characterization and photocatalytic activity under UV and visible light irradiation. *Appl Catal Gen* 2014;473:104–15.
- [88] Gao Z, Yang H, Mao J, Wu J. Construction of $\alpha\text{-Fe}_2\text{O}_3$ and Fe/Co-N₄ structures with faceted TiO_2 nanocrystals for highly efficient degradation of sulfathiazole in water. *J Clean Prod* 2019;220:668–76.
- [89] Mannaa MA, Qasim KF, Alshorifi FT, El-Bahy SM, Salama RS. Role of NiO nanoparticles in enhancing structure properties of TiO_2 and its applications in photodegradation and hydrogen evolution. *ACS Omega* 2021;6:30386–400.
- [90] Bootluck W, Chitrakarn T, Techato K, Jutaporn P, Khongnakorn W. S-scheme $\alpha\text{-Fe}_2\text{O}_3\text{/TiO}_2$ photocatalyst with Pd cocatalyst for enhanced photocatalytic H₂ production activity and stability. *Catal Lett* 2021. <https://doi.org/10.1007/s10562-021-03873-5>.